NANOPHOTONICS

Gate-tunable negative refraction of mid-infrared polaritons

Hai Hu[1,2]†*, Na Chen[1,2]†, Hanchao Teng[1,2]†, Renwen Yu[3], Mengfei Xue[6], Ke Chen[1,2], Yuchuan Xiao[1,2], Yunpeng Qu[1,2], Debo Hu[1,2], Jianing Chen[6], Zhipei Sun[7], Peining Li[8], F. Javier García de Abajo[4,5]*, Qing Dai[1,2]*

Negative refraction provides a platform to manipulate mid-infrared and terahertz radiation for molecular sensing and thermal emission applications. However, its implementation based on metamaterials and plasmonic media presents challenges with optical losses, limited spatial confinement, and lack of active tunability in this spectral range. We demonstrate gate-tunable negative refraction at mid-infrared frequencies using hybrid topological polaritons in van der Waals heterostructures. Specifically, we visualize wide-angle negatively refracted polaritons in α-MoO_3 films partially decorated with graphene, undergoing reversible planar nanoscale focusing. Our atomically thick heterostructures weaken scattering losses at the interface while enabling an actively tunable transition of normal to negative refraction through electrical gating. We propose polaritonic negative refraction as a promising platform for infrared applications such as electrically tunable super-resolution imaging, nanoscale thermal manipulation, enhanced molecular sensing, and on-chip optical circuitry.

Negative refraction has been extensively investigated in optics (*1*–*3*), nanoelectronics (*4*), acoustics (*5*), and magnetism (*6*) as a counter-intuitive physical phenomenon that holds strong potential for applications such as subwavelength imaging and cloaking (*7*). The past two decades have witnessed substantial progress in this field, with negative refraction demonstrations typically implemented using metallic metamaterials (*8*, *9*), dielectric photonic crystals (*10*, *11*), and hyperbolic metamaterials (*12*–*14*), composed of periodic arrays of subwavelength unit cells. The metamaterials invoked in these structures restrict their ability to strongly confine light. As an alternative, metal plasmons have also demonstrated negative refraction in the ultraviolet (*15*), visible (*16*), and near-infrared regions (*17*). This approach is limited by ohmic losses at visible and higher frequencies as well as by poor spatial confinement in the infrared range. Deep subwavelength negative refraction in the mid-infrared and terahertz domains has therefore remained a challenge despite its potential for sampling and controlling molecular vibrations and thermal radiation.

The emergence of van der Waals (vdW) materials has introduced a new degree of freedom in controlling light at the nanoscale over a wide spectral range by leveraging the strong optical confinement of their polaritonic modes (*18*–*22*). Recent theoretical studies have proposed the use of vdW polaritons to achieve deep subwavelength mid-infrared negative refraction, for example, in periodic arrays of graphene (*23*), or using planar graphene and hexagonal boron nitride (*h*-BN) heterostructures (*24*). Nevertheless, the extreme spatial confinement of polaritons in these structures hinders tailoring of their dispersions; reflection and scattering losses inherent to such structures also complicate the realization of theoretical concepts.

Results and discussion

We demonstrate deep subwavelength mid-infrared negative refraction by constructing a vdW heterostructure consisting of an α-MoO_3 film partially covered by monolayer graphene. Phonon polaritons (PhPs) in α-MoO_3 exhibit in-plane hyperbolic dispersion in the Reststrahlen band II from 816 to 972 cm^{-1}, where the permittivity components along the [100], [001], and [010] crystal directions satisfy $\varepsilon_x < 0$, $\varepsilon_y > 0$, and $\varepsilon_z > 0$, respectively (*25*–*28*) (note S1 and fig. S1). By contrast, graphene supports highly confined isotropic plasmons in this spectral region (*29*, *30*), such that anisotropic hyperbolic PhPs in the α-MoO_3 couple to graphene plasmons and results in an optical topological transition that allows us to flexibly engineer dispersion and isofrequency contours (IFCs) (*31*–*34*) (fig. S2).

By conserving the polariton wave vector along the direction of the interface (i.e., the

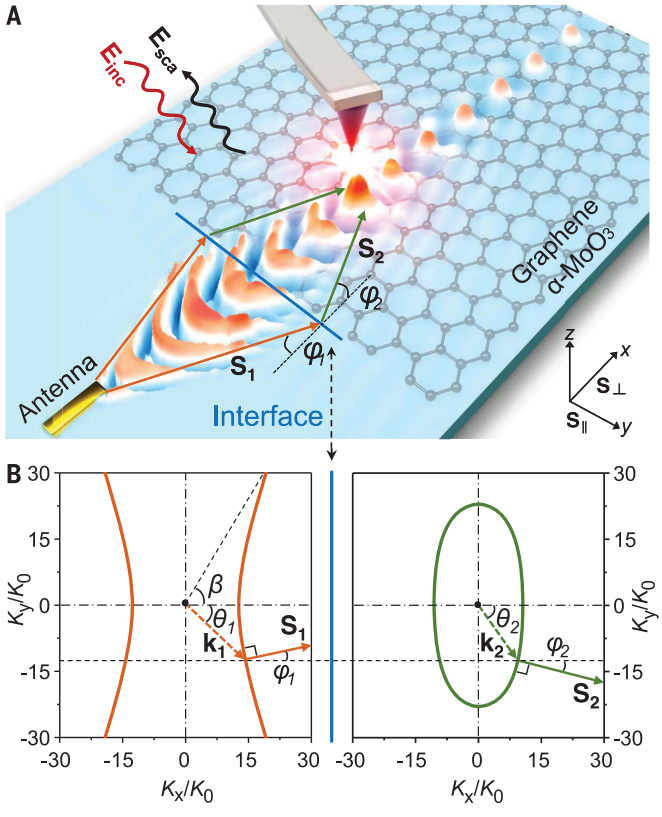

Fig. 1. Negative refraction of polaritons in two dimensions. (**A**) Schematics of the device. (**B**) IFCs of polaritons in hyperbolic (α-MoO_3) and elliptic (graphene/α-MoO_3) media. Negative refraction takes place at the interface between the two media as a result of conservation of the tangential wave vector. We define incidence and refraction angles θ_1 and θ_2 of the polaritons with wave vectors k_1 and k_2, respectively, as well as incidence and refraction angles φ_1 and φ_2 of the corresponding Poynting vectors S_1 and S_2, respectively. Angles are defined as positive (negative) on the upside (downside) of the direction normal to the interface.

[1]CAS Key Laboratory of Nanophotonic Materials and Devices, CAS Key Laboratory of Standardization and Measurement for Nanotechnology, CAS Center for Excellence in Nanoscience, National Center for Nanoscience and Technology, Beijing 100190, China. [2]Center of Materials Science and Optoelectronics Engineering, University of Chinese Academy of Sciences, Beijing 100049, China. [3]Department of Electrical Engineering, Ginzton Laboratory, Stanford University, Stanford, CA, USA. [4]ICFO-Institut de Ciencies Fotoniques, The Barcelona Institute of Science and Technology, 08860 Castelldefels (Barcelona), Spain. [5]ICREA-Institució Catalana de Recerca i Estudis Avançats, Passeig Lluís Companys 23, 08010 Barcelona, Spain. [6]The Institute of Physics, Chinese Academy of Sciences, P.O. Box 603, Beijing, China. [7]QTF Centre of Excellence, Department of Electronics and Nanoengineering, Aalto University, FI-02150 Espoo, Finland. [8]Wuhan National Laboratory for Optoelectronics and School of Optical and Electronic Information, Huazhong University of Science and Technology, Wuhan, China.
*Corresponding author. Email: daiq@nanoctr.cn, javier.garciadeabajo@nanophotonics.es, huh@nanoctr.cn
†These authors contributed equally to this work.

graphene edge), negative refraction is shown to take place when polaritons traverse the in-plane interface between the two regions (Fig. 1A). The Poynting vector S (directed along the energy flow, which is normal to the IFC) and the wave vector k are not collinear for non-circular IFCs (fig. S3 and note S2), such as those of hyperbolic polaritons in α-MoO_3 (Fig. 1B) (*35*). Because the boundary conditions at the interface (between α-MoO_3 with and without covering graphene) only require conservation of the tangential wave vector component $k_{\parallel} = k \sin\theta$, where θ is the angle between the wave vector and the direction normal to the interface, the refracted wave can exhibit normal (positive) refraction for k, but negative refraction for S (with $S_{\parallel} = S\sin\varphi$, where φ is the angle between the Poynting vector and the interface normal). Additional explanations regarding negative refraction are shown in fig. S4.

Negative refraction transforms the linear interface into a lens capable of focusing at a position determined from the relation between incidence and refraction angles, which can in turn be obtained by inspecting the distribution of the *z*-*z* component of the Dyadic Green function in real space and then comparing the Poynting vector S to the IFCs (see details in fig. S5 and note S3). Notably, because the IFCs possess inversion symmetry with respect to the graphene edge, negative refraction occurs reversibly when crossing the interface in both directions (i.e., to or from bare α-MoO_3).

For an experimental demonstration of negative refraction, we fabricated a gold antenna on one side of the interface (fig. S6) to serve as an excitation source of polaritons. Features of negative refraction are revealed by a scattering-type scanning near-field optical microscope equipped with a tunable quantum cascade laser (*36*, *37*). When hyperbolic PhPs are launched on the bare α-MoO_3 side and propagate toward the region covered by graphene, negative refraction occurs and the transmitted concave wavefront is observed to shrink sharply (Fig. 2, A and C). The focal point is situated at the fringe with the smallest full width at half maximum [(FWHM), the fifth fringe], yielding foci of FWHM as small as 373 nm (i.e., 1/30 of the free-space light wavelength) (Fig. 2E, right panel). After passing the focal spot, the wavefront begins to spread slightly in a diffractive fashion (sixth and higher order fringes).

We also demonstrate negative refraction when reversing the propagation direction by placing the launching antenna on the graphene/α-MoO_3 side (fig. S7), so that the diverging elliptic polaritons in such a medium are transmitted into converging hyperbolic PhPs in bare α-MoO_3 (Fig. 2, B and D), and a tightly squeezed focal spot (FWHM = 303 nm) is produced (Fig. 2E, right panel). After passing the focal point, the wavefront begins to spread slightly, but now with a hyperbolic wavefront. For a given set of polariton IFCs, the focusing effect can be modulated by moving the launching source, which produces a phase shift of the entire propagation wave (fig. S8).

The focusing concentrates the energy carried by polaritons to enhance the field intensity. Indeed, the square of the ratio of the electrical field at the focal spot to that without focusing yields an intensity increase by a factor of 10 (Fig. 2E and fig. S9). We note that losses related to refraction at the interface—which involve modal-profile mismatch between PhPs in α-MoO_3 and hybrid polaritons in graphene/α-MoO_3, as well as additional losses at the graphene edge—are relatively low (see details in figs. S10 and S11). Our experimental measurements agree well with simulated near-field distributions of Re{E_z} (Fig. 2, A and D) and the extracted simulation near-field profile also quantitatively matches the experimental data (fig. S9).

The reported in-plane negative refraction takes place over a wide range of incidence angles (Fig. 2F) as well as a wide spectral range, where the opening angle β of PhPs in α-MoO_3 increases with the illumination frequency, and the focal length varies in opposite ways with frequency for the two reversed refraction scenarios (figs. S12 and S13). For incidence or refraction in bare α-MoO_3, the incidence and refraction angles are both limited by the opening angle β as a result of PhPs propagation being prohibited beyond the IFC hyperbolic region, whereas negative refraction can be generated for a wide-angle range. Notably, in the Reststrahlen band III (higher light frequency from 958 to 1010 cm^{-1}), a lateral heterostructure can also achieve nanoscale negative refraction arising from the negative group velocity in the reversed dispersion of PhPs in α-MoO_3, whereas the actual experiment must take the impact of interface losses into account (*24*).

Active control and dynamic switching of negative refraction can be gained through electrostatic gating by varying the graphene chemical potential. We have demonstrated this possibility by preparing samples with a SiO_2/doped-Si substrate instead of Au, such that

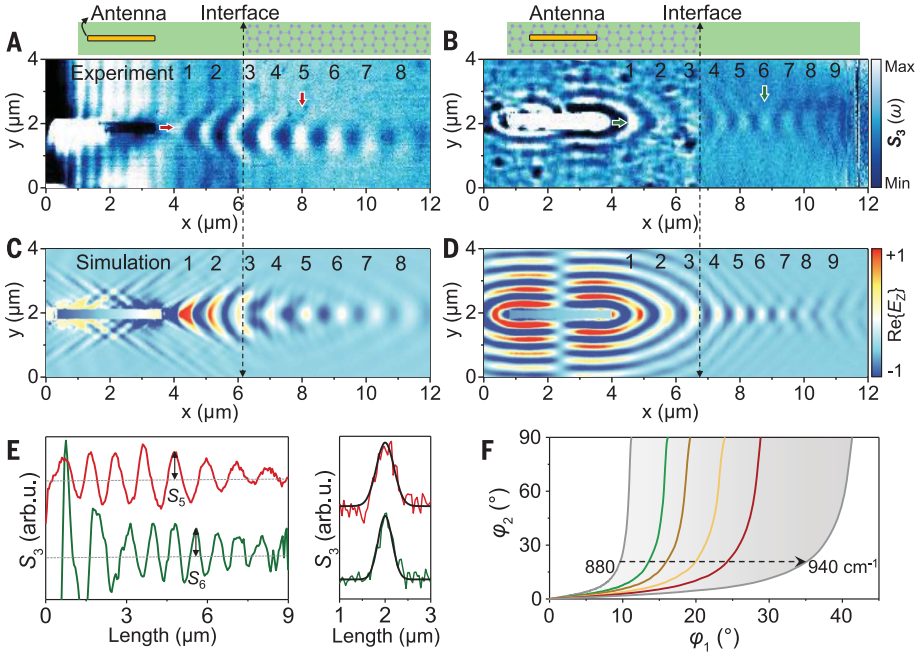

Fig. 2. Direct observation of nanoscale negative refraction. (**A** and **C**) Experimental (A) and simulated (C) near-field images illustrating negative refraction from a hyperbolic wave in α-MoO_3 to an elliptic wave in a graphene/α-MoO_3 heterostructure. (**B** and **D**) Negative refraction from elliptic to hyperbolic waves with the antenna now placed on the graphene/α-MoO_3 side. (**E**) Near-field profiles along the *x* (left) and *y* (right) directions [see red and green arrows in panels (A) and (B)]. Black curves in the latter are Gaussian fits of the transverse focal profile. All experimental results are measured from an in situ sample. The α-MoO_3 thickness is d = 242 nm. The graphene is mechanically exfoliated and statically doped to E_F = 0.5 eV by coverage with monolayer α-$RuCl_3$. The illumination frequency is ω_0 = 893 cm^{-1} (A) and 900 cm^{-1} (B), respectively. (**F**) Refraction (incidence) angle φ_2 in graphene/α-MoO_3 as a function of incidence (refraction) angle φ_1 in α-MoO_3 for various illumination frequencies from 880 to 940 cm^{-1} (gray shaded area). Color curves represent specific frequencies measured in our experiments.

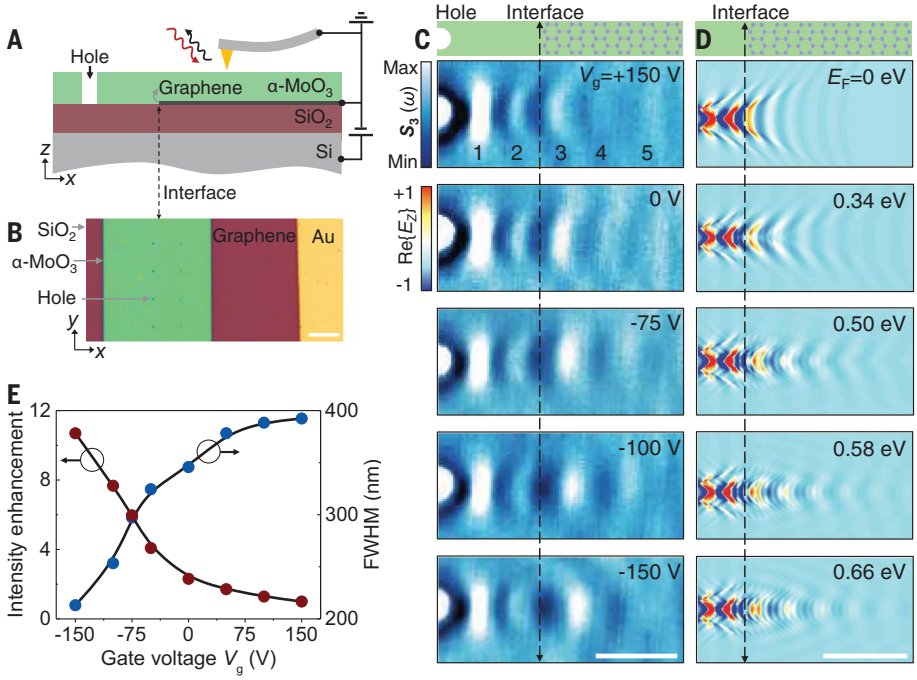

Fig. 3. Gate-tunable negative refraction. (**A**) Scheme of the gate-tunable device. (**B**) Optical image of a device consisting of an α-MoO_3 film, double-layer graphene, and SiO_2 substrate (from top to bottom). The diameter of the circular holes is 400 nm. (**C**) Experimentally measured near-field images of the transition from normal to negative refraction with gate voltages varying from +150 to −150 V. The vertical black dashed line represents the interface defined by the graphene edge. (**D**) Numerically simulated negative refraction with various Fermi energies of graphene from E_F = 0 to 0.66 eV, corresponding to the applied gate voltages. (**E**) Intensity enhancement (left) and FWHM (right) of the focal spots for various gate voltages, taken from the experimental measurements in (C). The α-MoO_3 thickness is d = 60 nm and the illumination frequency is fixed at 893 cm^{-1}. The scale bar indicates 10 μm (A), 0.5 μm (C), and 2.5 μm (D), respectively.

we can apply a perpendicular electric field to graphene through a SiO_2 dielectric layer coating a Si backgate (Fig. 3A). To obtain a clean interface, we have directly transferred an α-MoO_3 film with through holes on the graphene with prefabricated electrodes (Fig. 3B), where polaritons are excited by the tip and subsequently reflected by the hole edge.

The effect of changing gating voltage V_g on the polaritons is shown in Fig. 3C and fig. S15, where the Fermi energy is tuned over a wide range from E_F = 0 to ~0.66 electron volts (eV). By decreasing V_g, the open angle of the hyperbolic wavefront continues to shrink toward the canalization point for the graphene/α-MoO_3 region (figs. S15 and S16 and Fig. 3C), whereas the hyperbolic polaritons in bare α-MoO_3 show no response to the gate voltage (fig. S16A). This is attributable to a gradual switch on of negative refraction that originates in the topological transition of hybrid polaritons as holes are increasingly injected into graphene by lowering V_g. Our simulations further reproduce the continuous switching of negative refraction with varying doping levels of graphene (Fig. 3D and fig. S16B).

This gate-tunable negative refraction provides the capability to actively control the wavefront of polaritons in situ and change the focusing position and the corresponding optical fields at the nanoscale (Fig. 3, C and D). As the gate voltage changes from +150 to −150 V, the FWHM transverse size of the focal spot decreases and the focal field intensity increases by more than one order of magnitude (Fig. 3E and fig. S17). Figure S18 shows our gate-tunable negative refraction of another sample with monolayer graphene and thinner α-MoO_3, where the FWHM of the focal point reaches sizes as small as 185 nm (i.e., ~1/60 or 1.6% of the free-space light wavelength).

Negative refraction achieved by engaging topological polaritons with different IFC shapes is distinct from that attained by using bulk materials with a negative index of refraction (*8*). We are essentially relying on a homogeneous film (α-MoO_3) in which the addition of an atomically thin layer (graphene) radically changes the polaritonic mode characteristics to enable negative refraction. By changing the Fermi energy of graphene (and correspondingly, the composition of the topological hybrid polaritons), we can actively and continuously transition from normal to negative refraction (figs. S19 and S20 show how gate tuning of graphene affects negative refraction), whereas control of bulk materials remains a challenge. Note that, to achieve a high degree of negative refraction, the required doping level is relatively high. Therefore, we use double-layer graphene and adopt thinner α-MoO_3 films in Fig. 3 to decrease the demand for gate voltages, although this results in a shorter propagation distance than in the thicker sample in Fig. 2. To balance propagation distance and tunability range, more efficient double (top-and-back) gates (*38*) are promising for future investigations, possibly in combination with glass or ion gel spacers.

Conclusion

We have experimentally demonstrated a transition from normal to negative refraction in the mid-infrared spectral region by designing a vdW heterostructure consisting of an extended α-MoO_3 film that is half covered by monolayer graphene. The observed negative refraction over a wide range of incidence angles, which relies on topological polaritons with tunable dispersion curves, is revealed through real-space nanoimaging based on infrared nanoscopy. We leverage reversible negative refraction to demonstrate nanoscale focusing with either concave or convex wavefronts, which—because of the high spatial confinement of polaritons and the atomic thickness of the employed vdW structures—results in deep subwavelength focal spots with highly squeezed sizes of less than 60 times that of the corresponding illumination wavelength, more than tenfold intensity enhancement, and ~90% transmission of negatively refracted energy. Notably, we show that the transition from normal to negative refraction can be actively tuned by an electrostatic gate, resulting in the ability to control the wavefront of polaritons in situ and change focal spots and their nanoscale optical fields.

Considering the vast range of freshly available two-dimensional polaritonic materials, we anticipate negative refraction of polaritons in other vdW heterostructures involving, for example, α-V_2O_5, black phosphorus, and nanostructured metasurfaces (e.g., based on isotopically pure *h*-BN). The broad suite of existing materials could lead to polaritonic negative refraction covering the entire mid-infrared and terahertz region. The combined advantage of strong polariton-field confinement, flexible control over anisotropic polariton propagation and focusing, and tunability by material stacking as well as electric gating opens exciting avenues for negative refraction in optical and thermal applications.

REFERENCES AND NOTES

1. J. B. Pendry, *Phys. Rev. Lett.* **85**, 3966–3969 (2000).
2. R. A. Shelby, D. R. Smith, S. Schultz, *Science* **292**, 77–79 (2001).
3. J. Yao *et al.*, *Science* **321**, 930 (2008).

4. G.-H. Lee, G.-H. Park, H.-J. Lee, *Nat. Phys.* **11**, 925–929 (2015).
5. H. He *et al*., *Nature* **560**, 61–64 (2018).
6. A. Pimenov, A. Loidl, P. Przyslupski, B. Dabrowski, *Phys. Rev. Lett.* **95**, 247009 (2005).
7. W. Cai, U. K. Chettiar, A. V. Kildishev, V. M. Shalaev, *Nat. Photonics* **1**, 224–227 (2007).
8. D. R. Smith, J. B. Pendry, M. C. Wiltshire, *Science* **305**, 788–792 (2004).
9. K. L. Tsakmakidis, A. D. Boardman, O. Hess, *Nature* **450**, 397–401 (2007).
10. E. Cubukcu, K. Aydin, E. Ozbay, S. Foteinopoulou, C. M. Soukoulis, *Nature* **423**, 604–605 (2003).
11. P. V. Parimi, W. T. Lu, P. Vodo, S. Sridhar, *Nature* **426**, 404 (2003).
12. A. Poddubny, I. Iorsh, P. Belov, Y. Kivshar, *Nat. Photonics* **7**, 948–957 (2013).
13. J. S. Gomez-Diaz, A. Alù, *ACS Photonics* **3**, 2211–2224 (2016).
14. Q. Chen *et al*., *Photon. Res.* **9**, 1540–1549 (2021).
15. T. Xu, A. Agrawal, M. Abashin, K. J. Chau, H. J. Lezec, *Nature* **497**, 470–474 (2013).
16. H. J. Lezec, J. A. Dionne, H. A. Atwater, *Science* **316**, 430–432 (2007).
17. V. Podolskiy, A. Sarychev, V. Shalaev, *Opt. Express* **11**, 735–745 (2003).
18. A. Vakil, N. Engheta, *Science* **332**, 1291–1294 (2011).
19. D. N. Basov, M. M. Fogler, F. J. García de Abajo, *Science* **354**, aag1992 (2016).
20. T. Low *et al*., *Nat. Mater.* **16**, 182–194 (2017).
21. Q. Zhang *et al*., *Nature* **597**, 187–195 (2021).
22. Y. Wu *et al*., *Nat. Rev. Phys.* **4**, 578–594 (2022).
23. K. V. Sreekanth, A. De Luca, G. Strangi, *Appl. Phys. Lett.* **103**, 023107 (2013).
24. X. Lin *et al*., *Proc. Natl. Acad. Sci. U.S.A.* **114**, 6717–6721 (2017).
25. W. Ma *et al*., *Nature* **562**, 557–562 (2018).
26. Z. Zheng *et al*., *Sci. Adv.* **5**, eaav8690 (2019).
27. G. Hu *et al*., *Nature* **582**, 209–213 (2020).
28. M. Chen *et al*., *Nat. Mater.* **19**, 1307–1311 (2020).
29. J. Chen *et al*., *Nature* **487**, 77–81 (2012).
30. Z. Fei *et al*., *Nature* **487**, 82–85 (2012).
31. G. Álvarez-Pérez *et al*., *ACS Photonics* **9**, 383–390 (2022).
32. Y. Zeng *et al*., *Nano Lett.* **22**, 4260–4268 (2022).
33. F. L. Ruta *et al*., *Nat. Commun.* **13**, 3719 (2022).
34. H. Hu *et al*., *Nat. Nanotechnol.* **17**, 940–946 (2022).
35. G. Álvarez-Pérez *et al*., *Sci. Adv.* **8**, eabp8486 (2022).
36. P. Alonso-González *et al*., *Science* **344**, 1369–1373 (2014).
37. P. Li *et al*., *Science* **359**, 892–896 (2018).
38. Y. Zhang *et al*., *Nature* **459**, 820–823 (2009).

ACKNOWLEDGMENTS

This work was completed especially for the 20th anniversary of the National Center for Nanoscience and Technology, Beijing. The authors acknowledge the Nanofabrication Lab of NCNST for assistance in sample fabrication. **Funding:** This work was funded by the following: National Key Research and Development Program of China grant 2021YFA1201500 (to Q.D.); National Key Research and Development Program of China grant 2020YFB2205701 (to H.H.); National Natural Science Foundation of China grants 51902065 and 52172139 (to H.H.); National Natural Science Foundation of China grants 51925203 and U2032206 (to Q.D.); National Natural Science Foundation of China grant U2032206 (to Q.D.); National Natural Science Foundation of China grant 52072083 (to D.B.H.); National Natural Science Foundation of China grant 62075070 (to P.N.L.); Beijing Municipal Natural Science Foundation grant 2202062 (to H.H.); Beijing Nova Program grant 2022012 (to H.H.); Strategic Priority Research Program of Chinese Academy of Sciences grant XDB36000000 (to Q.D.); ERC grant 789104-eNANO (to F.J.G.A.); Spanish MICINN grants PID2020-112625GB-I00 and SEV2015-0522 (to F.J.G.A.); Academy of Finland grants 314810, 333982, 336144, 352780, 352930, and 353364 (to Z.P.S.); Academy of Finland Flagship Programme grant 320167, PREIN (to Z.P.S.); EU H2020-MSCA-RISE-872049 (IPN-Bio) (to Z.P.S.); ERC grant 834742 (to Z.P.S.). **Author contributions:** Conceptualization: Q.D., F.J.G.A., and H.H. Supervision: Q.D. and F.J.G.A. Funding acquisition: Q.D., H.H., F.J.G.A., Z.P.S., P.N.L., and D.B.H. Experimentation: H.H. and N.C. Theory and simulation: H.C.T., R.W.Y., and F.J.G.A. Data Analysis: H.H., N.C., and H.C.T. Writing – original draft: H.H., N.C., H.C.T., and Q.D. Writing – review and editing: H.H., N.C., H.C.T., Q.D., F.J.G.A., Z.P.S., P.N.L., J.N.C., R.W.Y., D.B.H., Y.P.Q., M.F.X., K.C., and Y.C.X. **Competing interests:** The authors declare no competing interests. **Data and materials availability:** The data that support the findings of this study are all available and archived in the main text or the supplementary materials.

SUPPLEMENTARY MATERIALS

science.org/doi/10.1126/science.adf1251
Materials and Methods
Notes S1 to S3
Figs. S1 to S21
Table S1
References (*39*–*44*)

Submitted 30 September 2022; accepted 13 January 2023
10.1126/science.adf1251